ER–mitochondria contacts orchestrate mitochondrial transport via C19orf12/EMTOR

Xiayuhe Pei[1,*], Shuqian Zhang[2,*], Peiyang Li[3], Yutong Wu[1], Yiru Cheng[1], Xia Feng[4,5], Yiqian Wu[3], Xiaoshuai Huang[6], Ning Huang[7,8], Bei Liu[3], Junlin Teng[1], Jianguo Chen[1,9,#], Craig Blackstone[4,5,#], Pengli Zheng[1,2,10,#]

[1]Key Laboratory of Cell Proliferation and Differentiation of the Ministry of Education, State Key Laboratory of Membrane Biology, School of Life Sciences, Peking University, Beijing 100871, China

[2]Peking-Tsinghua Center for Life Sciences, Academy for Advanced Interdisciplinary Studies, Peking University, Beijing 100871, China

[3]National Biomedical Imaging Center, College of Future Technology, Peking University, Beijing 100871, China

[4]MassGeneral Institute for Neurodegenerative Disease, Massachusetts General Hospital, Charlestown, MA 02114, USA

[5]Department of Neurology, Massachusetts General Hospital and Harvard Medical School, Boston, MA 02114, USA

[6]Beijing Advanced Center of Cellular Homeostasis and Aging-Related Diseases, Institute of Advanced Clinical Medicine, Peking University, Beijing,100191, China.

[7]Institute of Neuroscience, Translational Medicine Institute, Health Science Center, Xi'an Jiaotong University, Xi'an 710061, China

[8]Department of Physiology and Pathophysiology, School of Basic Medical Sciences, Health Science Center, Xi'an Jiaotong University, Xi'an 710061, China

[9]Center for Quantitative Biology, Academy for Advanced Interdisciplinary Studies, Peking University, Beijing 100871, China

[10]Lead contact

*These authors contributed equally to this work.

‡ Correspondences:

Jianguo Chen: chenjg@pku.edu.cn

Craig Blackstone: cblackstone@mgh.harvard.edu

Pengli Zheng: zhengpl@pku.edu.cn

Abstract

Endoplasmic reticulum (ER)–mitochondria contact sites facilitate lipid transfer, calcium signaling, and mitochondrial division, yet their role in mitochondrial transport remains unclear. Here, we identify Hereditary Spastic Paraplegia (HSP)-associated protein C19orf12 as an ER-anchored protein that acts as a central organizer for mitochondrial trafficking and rename it EMTOR (ER–Mitochondria Transport Organizer). In cells and mice, loss of EMTOR leads to severe perinuclear mitochondrial clustering, diminished axonal mitochondrial density, and progressive locomotor dysfunction recapitulating key features of HSP. Mechanistically, EMTOR forms a discrete complex with the mitochondrial Rho GTPase Miro1 and the kinesin-1 motor KIF5B, independently of the canonical TRAK adaptors, thereby directly linking ER–mitochondria contact sites to microtubule-based anterograde transport. This interaction is dynamically regulated by local calcium levels: enhanced at Ca^{2+} concentrations (1–10 μM) characteristic of ER–mitochondria contact microdomains, coinciding with increased mitochondrial speed, but markedly suppressed under high calcium conditions, correlating with mitochondrial transport arrest. Therefore, our findings establishes ER-mitochondria contact sites as logistical hubs for Kinesin-1 motor loading and highlights the importance of the calcium-tunable EMTOR scaffold in sustaining directional mitochondrial transport, revealing how the loss of this regulation drives the neurodegenerative cascade in HSP.

Key words: ER–mitochondria contact sites; Mitochondrial transport; C19orf12/EMTOR; Miro1; Kif5b; Hereditary Spastic Paraplegia

Introduction

Cells continuously adjust the dynamic distribution of their organelles through intracellular transport to ensure the efficient and orderly execution of cellular activities. Among these, mitochondria are essential metabolic hubs that participate in key cellular processes such as ATP production, calcium buffering, and apoptosis[1–3]. Mitochondrial transport is critical for cells to maintain spatial energetic and metabolic balance, and is particularly indispensable for highly specialized cells with extended morphologies and intense energy demands, most notably neurons[2–5]. Neurons possess elongated axons and rely on precise mitochondrial delivery to distal synapses to sustain synaptic transmission, plasticity, and survival. Consequently, aberrant mitochondrial transport is a hallmark of neurodegenerative disorders, including Alzheimer's disease, Parkinson's disease, and Hereditary Spastic Paraplegia (HSP) [6–8].

Mitochondrial trafficking is driven by a diverse repertoire of molecular motors and adaptors. Long-range anterograde transport is primarily mediated by microtubule-based kinesin-1 (KIF5) and kinesin-3 (KIF1B)[9], while retrograde movement relies on cytoplasmic dynein[10,11]. Beyond these long-range transporters, short-range motility in actin-rich domains utilizes Myosin19[12,13], and stationary retention is enforced by the axonal docking factor Syntaphilin (SNPH)[4,14]. These motors are coupled to the mitochondrial surface via adaptor complexes, including the Metaxins[15] and, most notably, the mitochondrial Rho GTPases (Miro1/2)[16,17] and trafficking kinesin-binding proteins (TRAK1/2)[18–21]. A fundamental question thus arises: how does the cell spatially coordinate these ubiquitous motors and adaptors to ensure mitochondria are mobilized or anchored at the right time and place?

A critical regulatory feature of this machinery centers on Miro1, which harbors EF-hand motifs to sense cytosolic Ca^{2+} (cCa^{2+}). An increase in local cCa^{2+} is widely recognized to act as a "stop signal" that inhibits mitochondrial movement, particularly in neurons. Although this arrest involves Ca^{2+}-induced conformational changes in Miro1, the exact structural basis for motor inhibition is not fully understood, as studies have variously proposed either the decoupling of kinesin from its cargo or the direct impediment of motor–microtubule attachment[22,23]. Additionally, this process is further modulated by interactions with the mitochondrial calcium uniporter (MCU) and matrix calcium dynamics[24,25]. However, distinct from these inhibitory mechanisms, the role of basal physiological Ca2+ levels remains less defined, with emerging evidence suggesting that specific calcium concentrations may be required for complex integrity rather than solely acting as a stop signal[25–28].

The endoplasmic reticulum (ER), the largest membranous organelle in the cell, functions as a central platform for organelle communication[29]. Through extensive membrane contact sites (MCSs), the ER orchestrates essential physiological processes, including calcium transfer[30], lipid exchange[31], and mitochondrial fission–fusion dynamics[32,33]. Previous work from our laboratory has demonstrated that the structural distribution of the ER broadly dictates the spatial organization of other membrane-bound organelles[34]. This suggests that the ER may play a central, yet underappreciated, role in governing organelle transport. Crucially, specific ER-resident proteins can actively drive this organization; for instance, Protrudin has been shown to simultaneously bind Kinesin-1 and the endosomal protein Rab7, thereby acting as a scaffold to promote the anterograde

transport of lysosomes and late endosomes[35]. Recent studies have further suggested that ER tubules can mechanically guide mitochondrial positioning via "hitchhiking" mechanisms[36]. Notably, the enrichment of Miro1 at ER–mitochondria interfaces[37] suggests that ER-resident proteins may actively regulate mitochondrial motility. However, whether ER proteins directly recruit or regulate the transport machinery remains unknown.

Hereditary Spastic Paraplegia (HSP) provides a compelling genetic window into this potential ER-transport link. HSP is characterized by the length-dependent degeneration of corticospinal motor neurons, leading to progressive lower limb spasticity[38]. Strikingly, over 60% of pathogenic HSP mutations occur in ER-shaping or ER-resident proteins (e.g., Atlastins, REEPs, Spastin[38]), implicating ER dysfunction as a primary driver of axonopathy. Yet, the downstream consequence of these ER mutations often manifests as defects in axonal transport and mitochondrial distribution[39]. This disconnect suggests that critical molecular linkers connecting the ER network to the mitochondrial transport machinery are missing from our current understanding.

C19orf12, a gene mutated in a severe form of HSP (SPG43), represents a candidate for this missing link[40–42]. Previous studies have reported that C19orf12 localizes to both the ER and mitochondria under overexpression conditions and implicated the protein in broad cellular process including autophagy and lipid metabolism[43,44]. However, the precise subcellular localization of the endogenous protein remains controversial, and its primary physiological function—specifically the molecular mechanism linking its dysfunction to axonal degeneration—remains elusive. Here, we identify C19orf12 as an ER-anchored organizer of mitochondrial transport complex that enriches at ER-mitochondria contact sites. Based on these distinct characteristics, we propose to rename this protein **EMTOR** (**E**ndoplasmic reticulum–**M**itochondria **T**ransport **Or**ganizer). We demonstrate that EMTOR is indispensable for maintaining axonal integrity, as its deficiency drives progressive motor impairment in mice and distal mitochondrial depletion in neurons.Mechanistically, we reveal that EMTOR functions as a Ca^{2+}-tunable scaffold that bridges the ER to the mitochondrial surface, promoting the assembly of the Miro1–Kinesin-1 complex. Our findings reveal that ER-mitochondria contacts serve as critical logistical hubs for organelle transport, providing a unifying mechanism for the pathogenesis of HSP.

Results

EMTOR deficiency leads to progressive motor impairment and HSP-like pathology in mice

To determine the physiological function of the HSP-associated protein EMTOR (encoded by *C19orf12*), we generated constitutive knockout mice (*Emtor*$^{-/-}$, **Fig 1a, Extended Data Fig. 1a, b**). We first characterized the expression profile of EMTOR in the brain. RT-qPCR and Immunoblotting of wild-type lysates revealed that EMTOR expression progressively increases during postnatal development (from P5 to P60), coinciding with the period of neuronal maturation **(Extended Data Fig. 1c, d)**.

Clinically, *C19orf12* mutations cause Spastic Paraplegia type 43 (SPG43), characterized by progressive spasticity and motor dysfunction. Our mouse model robustly recapitulated these features. While young mice appeared normal, aged *Emtor*$^{-/-}$ mice (15 months) developed pronounced hindlimb clasping reflexes and abnormal gait patterns indicative of pyramidal tract dysfunction **(Fig. 1a–d)**. Comprehensive behavioral testing revealed significant deficits in motor coordination and neuromuscular strength: knockout mice showed reduced latency on the rotarod, increased time to descend the pole, difficulty in the beam-walking test, and weakened grip strength compared to age-matched controls **(Fig. 1e)**. Although active motor challenges were terminated, we continued to monitor spontaneous behaviors and general health longitudinally. Automated gait analysis in aged mice revealed a higher stride Symmetry Index (SI stride) and increased Coefficient of Variation (CV base), quantitatively confirming persistent gait instability **(Fig. 1f, g)**.

Furthermore, longitudinal monitoring revealed a late-onset systemic phenotype, characterized by progressive weight loss and increased mortality in *Emtor*$^{-/-}$ geriatric mice **(Fig. 1h-j)**. These data establish *Emtor*$^{-/-}$ mice as a valid model for HSP and indicate that EMTOR is essential for maintaining long-term motor function.

EMTOR is essential for axonal mitochondrial transport and bioenergetics in hippocampal neurons

We next investigated the cellular basis of these motor deficits. HSP is characterized by the specific degeneration of long corticospinal axons, a "dying-back" pathology strongly implicating defects in long-range axonal transport[38,39]. Given the crucial role of mitochondria in sustaining synaptic energy homeostasis[4], we hypothesized a defect in axonal mitochondrial transport. In primary hippocampal neurons isolated from *Emtor*$^{-/-}$mice, time-lapse imaging revealed a severe impairment in mitochondrial motility **(Fig. 2a)**. While wild-type neurons displayed robust bidirectional movement, knockout neurons exhibited a marked reduction in the fraction of motile mitochondria and a corresponding increase in stationary states **(Fig. 2a, b)**. This phenotype was further validated using acute shRNA-mediated knockdown of EMTOR in wild-type neurons, which recapitulated the transport defects **(Extended Data Fig. 1e, f)**. A direct consequence of failed anterograde transport is the inability to replenish mitochondria at distal sites. Indeed, imaging of axonal terminals (marked by Tau) revealed a progressive depletion of mitochondria towards the distal end in knockout neurons compared to controls **(Fig. 2c)**. Quantification of mitochondrial fluorescence intensity specifically within axonal tips confirmed a significant reduction in mitochondrial payload **(Fig. 6d; Extended Data Fig. 1g, h)**.

Mitochondria are essential for local ATP synthesis to fuel synaptic transmission. We therefore asked whether this spatial depletion compromised neuronal bioenergetics. Using the ratiometric ATP probe GO-ATeam2 (single-excitation, dual-emission readout), we detected lower ATP levels (F560/F510 ratio) at distal axons/terminals in both knockout and knockdown neurons to controls **(Fig. 2e, f; Extended Data Fig. 1i, j)**. Collectively, these data demonstrate that EMTOR is indispensable for sustaining the population of motile mitochondria required to supply the distal axon and maintain neuronal energy homeostasis.

EMTOR deficiency induces perinuclear mitochondrial clustering

To dissect the molecular mechanism underlying this transport defect, we utilized U2OS cells as a tractable models since EMTOR is broadly expressed across tissues[45] **(Extended Data Fig. 2a)**. Consistent with the neuronal phenotype, loss of EMTOR resulted in a striking redistribution of the mitochondrial network: mitochondria retracted from the cell periphery and accumulated heavily in the perinuclear region **(Fig. 3a, b)**. Quantitative analysis using asymmetry coefficient confirmed a significant reduction in mitochondrial spreading **(Fig. 3c)**, and the proportion of cells exhibiting severe clustering increasing from ~25% in wild-type (WT) to ~80% in U2OS KO cells **(Fig. 3d)**. Importantly, the distribution of lysosomes (LAMP1) remained unaffected **(Fig. 3a, c, d)**, and lysosomal marker levels were stable **(Extended Data Fig. 2b)**. Furthermore, mitochondrial membrane potential ($\Delta\psi m$) was preserved in KO cells **(Extended Data Fig. 2c, d)**.

To link this phenotype to HSP pathology, we performed rescue experiments with human *EMTOR* variants[40,42]. Re-expression of full-length EMTOR in KO cells fully restored the peripheral mitochondrial network whereas pathogenic mutants G58R and A63P, which were diffuse in the cytosol, failed to rescue the phenotype **(Fig. 3e-g; Extended Data Fig. 2e)**. Notably, the A34V mutant retained ER localization similar to WT but still failed to reinstate normal distribution **(Fig. 3e)**. This result implies that while membrane targeting is necessary, it is insufficient for function; the A34V mutation likely disrupts a specific effector interaction required for mitochondrial positioning. Validation in other cell lines confirmed that this clustering phenotype was conserved across multiple cell types, including COS7 and A549 cells **(Extended Data Fig. 3)**.

Crucially, to determine whether these transport defects in mice and cells were secondary to the degradation of transport machinery, we analyzed protein abundance. Immunoblotting of whole brain and spinal cord lysates from *Emtor*$^{-/-}$ mice, as well as lysates from *EMTOR* KO cells, revealed that the total levels of key transport components (Miro1, Kif5b, KLCs) and mitochondrial markers (Tom20) remained unchanged **(Extended Data Fig. 4)**. This confirms that the observed phenotypes arise from the functional impairment of the transport machinery rather than the loss of its components.

EMTOR is a dynamic ER-anchored protein enriched at ER–mitochondria contact sites

Having established that EMTOR deficiency causes mitochondrial clustering, we next sought to define its precise subcellular localization and dynamics to understand how it exerts this spatial control. Consistent with previous reports[41], overexpressed EMTOR showed both ER and mitochondrial localization **(Extended Data**

Fig. 5a). To test this at the endogenous level without overexpression artifacts, we established *EMTOR*-Halo-3×Flag and *EMTOR*-ALFA knock-in U2OS cells using CRISPR-Cas9. In endogenous level, all EMTOR signals co-localize with ER marker Sec61β, with slight enrichment at ER-mitochondrial contact sites **(Fig. 4a; Extended Data Fig. 5b)**, suggesting that EMTOR is an ER-associated protein that specifically functions at the interface between these two organelles.

However, standard subcellular fractionation[46] yielded a paradoxical result: while the protein appeared ER-associated in imaging, biochemical analysis of U2OS and HEK293T lysates showed that the vast majority of EMTOR in the cytosolic fraction, with minimal signal in the crude mitochondrial (Mc) or ER-enriched fractions **(Extended Data Fig. 5c, d)**. This discrepancy suggested that EMTOR might be loosely or dynamically associated with the ER membrane, making it susceptible to dissociation during cell lysis. To test this hypothesis, we performed fractionation following crosslinking to stabilize transient interactions. Strikingly, under crosslinking conditions, the endogenous EMTOR pool shifted from the cytosolic fraction to the ER-bound fractions **(Fig. 4b)**. Single-molecule tracking (SMT) further confirmed that EMTOR molecules diffuse along ER tubules but exhibit transient confinement specifically at regions overlapping with mitochondria **(Fig. 4c)**.

Collectively, these biochemical and biophysical data demonstrate that EMTOR is not a stable integral transmembrane protein, but rather a dynamic ER-anchored protein that transiently accumulates at ER–mitochondria contact sites.

ER membrane anchoring is necessary and sufficient for EMTOR function

To test if ER anchoring is required for function, we performed rescue experiments with chimeric constructs. A mutant lacking the previously predicted hydrophobic transmembrane-like region (ΔpTM) failed to rescue mitochondrial clustering **(Fig. 4d–g)**. Our earlier biochemical and imaging data **(Fig. 3b, c; Extended Data Fig. 5c, d)** have established that EMTOR is not an integral membrane protein, and this predicted hydrophobic region does not function as a canonical transmembrane domain. However, the loss-of-function phenotype of the ΔpTM mutant indicates that this hydrophobic region is critical for EMTOR's dynamic association with the ER membrane. Collectively, these results confirm that ER membrane association—mediated by the predicted hydrophobic region—is essential for EMTOR's ability to regulate mitochondrial distribution.

To further confirm that ER anchoring is indispensable for EMTOR's function, we next tested whether replacing its native hydrophobic region with heterologous ER-targeting sequences could substitute for the endogenous motif. We generated chimeric EMTOR constructs by replacing the predicted hydrophobic region with ER-targeting transmembrane domains from Atlastin-3 (ATL3-TM) or EI24 (EI24-TM), while also generating a control construct targeting EMTOR to the mitochondrial outer membrane using the MFN2 transmembrane domain (MFN2-TM). Remarkably, the ER-anchored chimeric constructs (ATL3-TM and EI24-TM) fully rescued the mitochondrial distribution defects in EMTOR KO cells. In contrast, the mitochondria-targeted MFN2-TM chimeric construct failed to restore normal mitochondrial spreading (**Fig. 2d-g; Extended Data Fig. 3d)**.

Thus, we conclude that EMTOR function is strictly dependent on its specific localization to the ER membrane, as artificial ER targeting—but not mitochondrial targeting—is critical to rescue the transport defects.

EMTOR is required for Kinesin-1 recruitment and interacts with the mitochondrial transport machinery

The severe perinuclear clustering of mitochondria observed in *EMTOR*-KO cells suggests a specific deficit in anterograde transport. We therefore hypothesized that EMTOR loss might impair the recruitment of the anterograde motor Kinesin-1 heavy chain (Kif5b). To test this, we visualized the endogenous association between motor proteins and mitochondria using the Proximity Ligation Assay (PLA). Strikingly, the PLA signals representing the interaction between Kif5b and the mitochondrial marker TOM20 were drastically reduced in *EMTOR*-KO cells and *Emtor*$^{-/-}$ *brain* tissues **(Fig. 5a-d)**. In contrast, the interaction between Dynein and mitochondria remained unchanged in *EMTOR*-KO cells **(Fig. 5a, b).** This indicates that EMTOR is specifically required for the attachment of the anterograde transport machinery.

To identify the molecular machinery engaged by EMTOR, we performed affinity purification-mass spectrometry (AP-MS) using purified EMTOR as bait **(Extended Data Fig. 6a)**. This unbiased screen identified Kif5b and the mitochondrial Rho GTPase Miro1/2 as potential interactors of EMTOR **(Extended Data Fig. 6b)**. Given the high sequence homology between the two Rho GTPases and the higher peptide coverage observed for Miro1, we focused our mechanistic characterization on Miro1 as the representative isoform.

To validate these interactions and confirm their specificity, we first performed co-immunoprecipitation (Co-IP) assays. These demonstrated robust interactions between EMTOR and both Miro1 and Kif5b **(Fig. 5e, f).** Notably, the canonical mitochondrial adaptor TRAK1 was absent from the EMTOR interactome, and Co-IP assays further confirmed that EMTOR does not physically associate with TRAK1 **(Extended Data Fig. 6c)**, indicating that EMTOR engages the transport machinery through a distinct, specific interface rather than binding promiscuously to all transport adaptors. Importantly, we revisited the HSP-associated A34V mutant. Although this mutant localizes correctly to the ER, it exhibited significantly reduced binding affinity for both Miro1 and Kif5b **(Fig. 5e, f)**. This molecular defect—the inability to effectively recruit the motor complex—provides a mechanistic explanation for why the A34V variant fails to support mitochondrial transport and causes disease.

To further confirm the EMTOR-Miro1-Kif5b interactions at endogenous levels, we utilized U2OS cells harboring a knock-in 3×Flag-Miro1 allele. Under DSP cross-linking conditions, endogenous EMTOR co-immunoprecipitated with Miro1 **(Fig. 5g)**. This interaction was preserved under mild detergent conditions while simultaneously recovering the known Miro1–Kif5b/TRAK1/TRAK2 assemblies **(Fig. 5h)**, confirming physiological complex formation.

Furthermore, *in vitro* pull-down assays using purified recombinant proteins confirmed that EMTOR acts as a direct physical linker, binding directly to both Miro1 and Kif5b **(Fig. 5i, j)**. Detailed domain mapping using truncation mutants revealed distinct binding modes for these partners: EMTOR specifically recognizes the C-

terminal cargo-binding tail of Kif5b (amino acids 744–963)—the canonical site for adaptor attachment—whereas it engages Miro1 through a more complex, extensive interface involving multiple structural domains. **(Extended Data Fig. 6d-j)**.

Intriguingly, during these biochemical characterizations, we observed that purified EMTOR protein formed spherical droplets under molecular crowding conditions exhibiting fusion and fission dynamics, characteristic of liquid-liquid phase separation (LLPS) (Extended Data Fig. 7a, Extended Data Fig. 8a, b). In contrast, neither Miro1 nor Kif5b formed condensates on their own under identical conditions (Extended Data Fig. 7b, c). However, EMTOR was able to recruit both Miro1 and Kif5b into these condensates (Extended Data Fig. 7d, Extended Data Fig. 8c-g), suggesting that the transport machinery might be assembled within specialized phase-separated compartments at contact sites.

EMTOR scaffolds the assembly of the Miro1–Kinesin-1 anterograde transport complex

Having established that EMTOR directly binds the transport machinery, we investigated why its loss leads to motor detachment. Mechanistically, we hypothesized that EMTOR acts as a scaffold to stabilize the Miro1–Kif5b complex. Consistent with this, the interaction between Miro1 and Kif5b was significantly reduced in *EMTOR*-KO cells compared to WT controls **(Fig. 5k, l)**. Moreover, in the in vitro binding assays, the presence of EMTOR promoted the association between Kif5b and Miro1 **(Fig. 5m)**. These data demonstrate that EMTOR is essential for the efficient assembly of the Miro1–Kinesin-1 complex.

To define the pathway specificity and hierarchy of EMTOR, we examined its relationship with the canonical transport adaptors Miro1 and TRAK1. Given that EMTOR does not physically bind TRAK1 **(Extended Data Fig. 6c)**, we asked if they function through independent mechanisms. Overexpression of TRAK1 is known to drive mitochondrial hyper-spreading[21,47]. We found that TRAK1 overexpression induced mitochondrial extension not only in WT cells but also in *EMTOR*-KO cells to a similar extent **(Extended Data Fig. 9a-c)**. This ability of TRAK1 to bypass EMTOR deficiency indicates that EMTOR functions independently of the TRAK1-mediated transport pathway.

In contrast, we observed a distinct dependency relationship with Miro1. While overexpression of Miro1 induced a slight outward displacement of mitochondria and promoted hyper-fusion[17], it failed to effectively restore the global mitochondrial spreading in *EMTOR*-KO cells **(Extended Data Fig. 9d-f)**. This suggests that increasing Miro1 dosage alone is insufficient to drive long-range transport in the absence of EMTOR, and that Miro1 requires EMTOR to function effectively. Furthermore, to determine if EMTOR could compensate for the loss of core adaptors, we utilized *Miro1/2* double-knockout cells, which exhibited severe mitochondrial clustering[21,48] **(Extended Data Fig. 9g-i)**. These results indicate that EMTOR acts as a critical regulator that facilitates the assembly of the Miro1 complex but cannot bypass the loss of core components or substitute for their essential functions.

Ca^{2+} regulates EMTOR-mediated transport assembly and mitochondrial motility

Miro1 contains calcium-sensing EF-hand motifs, and previous studies have suggested that binding of cytosolic Ca^{2+} to Miro1 can trigger mitochondrial arrest[22,23]. Given this potential regulatory link, we hypothesized that the EMTOR-mediated assembly might be sensitive to calcium fluctuations. To explore this, we examined the transcriptional landscape of *EMTOR*-deficient cells. RNA-seq analysis revealed that "calcium ion binding" was among the top upregulated functional categories in *EMTOR*-KO cells **(Extended Data Fig. 10)**. This transcriptional signature hinted at a potential compensatory response to altered calcium handling, prompting us to test if Ca^{2+} directly regulates the EMTOR machinery.

We performed *in vitro* GST pull-down assays in the presence of varying free Ca^{2+} concentrations ranging from 0 (EGTA) to 1 mM **(Fig. 6a)**. Quantification revealed a "bell-shaped" binding dependence: the affinity between EMTOR and Miro1 increased from basal levels to a maximum at ~1 μM Ca^{2+} and declined at higher concentrations **(Fig. 6a, b)**. Notably, previous studies have estimated that local Ca^{2+} concentrations at ER–mitochondria contact sites fluctuate within the micromolar range (typically 1–20 μM) during signaling events. This suggests that physiological Ca^{2+} levels promote complex formation, whereas supraphysiological levels are inhibitory.

Consistent with this binding affinity data, we found that the phase separation of the complex is also exquisitely tuned by calcium. Crucially, the phase separation of EMTOR protein alone was unaffected by calcium fluctuations, maintaining stable droplets across all tested concentrations (Extended Data Fig. 11a-c). However, the formation of EMTOR–Miro1 co-condensates was significantly enhanced at physiological Ca^{2+} concentrations (~1–10 μM) but was suppressed under calcium-free or calcium-overload conditions (Extended Data Fig. 11d-i). This indicates that calcium acts as a specific switch to regulate the recruitment of the transport machinery rather than the structural integrity of the EMTOR scaffold itself.

To confirm that this regulation relies on the calcium-sensing ability of Miro1, we generated a Miro1 mutant with disrupted EF-hand domains (Miro1-ΔEF). Strikingly, the interaction between EMTOR and Miro1-ΔEF became insensitive to calcium fluctuations, maintaining a constant binding affinity across all tested concentrations **(Fig. 6c, d)** This explicitly demonstrates that Miro1 acts as the calcium sensor that tunes the assembly of the transport machinery.

To validate the physiological relevance of this regulation in living cells, we examined the relationship between local calcium dynamics and mitochondrial motility using the mitochondrial surface-localized calcium sensor GCaMP6f-Tom5 **(Fig. 6e)**. Live-cell time-lapse imaging revealed that mitochondria exhibit spontaneous, transient calcium "flashes" on their surface. By tracking individual mitochondria, we observed a statistically significant negative correlation between surface calcium intensity and movement speed: mitochondria typically displayed rapid motility during periods of low surface calcium, while slowing down or pausing during calcium spikes **(Fig. 6e-h)**.

Notably, while this correlation is significant, the linear regression analysis (R^2=0.03) indicates that surface calcium levels explain only a portion of the variability in mitochondrial speed **(Fig. 6h)**. This observation aligns with the consensus that mitochondrial transport is a highly complex process regulated by a multifactorial

network. In addition to calcium dynamics, motility is governed by local ATP availability, the engagement of opposing motors (Kinesin vs. Dynein), and the status of docking proteins (e.g., Syntaphilin)[4,11,14,20]. Therefore, our data posit physiological surface calcium as a critical rheostat that tunes the EMTOR-Miro1 assembly probability, functioning as one key layer of control within the broader regulatory landscape of mitochondrial trafficking.

Discussion

Our study uncovers the molecular mechanism of *C19orf12*, a gene linked to neurodegeneration[41,42], identifying its protein product as an ER-anchored regulator that confers precise ER-mediated control over mitochondrial transport. Based on its essential role in orchestrating these organelle dynamics, we refer to this protein as EMTOR. By delineating the function of EMTOR, we establish mitochondrial transport regulation as a novel functional dimension of ER–mitochondria contact sites, expanding their role beyond the canonical functions of lipid transfer and calcium signaling[31]. By combining mouse genetics, neuronal physiology, and biochemical reconstitution, we demonstrate that loss of EMTOR leads to a "dying-back" depletion of axonal mitochondria, energetic failure at synapses, and the progressive spastic paraplegia phenotype characteristic of HSP.

Our *Emtor* knockout mice robustly recapitulate the clinical features of SPG43, including progressive spasticity, muscle weakness, and gait instability[41]. These phenotypes mirror the late-onset motor impairment recently reported in another *Emtor*-deficient model[49], confirming that EMTOR is indispensable for the long-term maintenance of the corticospinal tract. At the cellular level, we pinpoint the primary defect to a failure in anterograde mitochondrial transport. This transport deficit creates a "supply chain crisis" in long axons: while the soma retains a clustered mitochondrial mass, distal terminals become devoid of organelles and depleted of ATP. This spatial bioenergetic mismatch offers a parsimonious explanation for the length-dependent degeneration of axons in HSP, linking the molecular defect in EMTOR directly to the vulnerability of distal synapses[8,38].

A central finding of our work is the definition of EMTOR's molecular identity as a dynamic ER-anchored scaffold. Previous studies relying on overexpression often observed EMTOR on both ER and mitochondria, leading to ambiguity about its primary site of action[41]. By leveraging endogenous tagging and single-molecule tracking, we show that physiological EMTOR resides on the ER membrane, concentrating transiently at contact sites. Crucially, our chimeric rescue experiments provide compelling evidence that ER anchoring is the critical spatial determinant for EMTOR function. Targeting EMTOR to the mitochondrial outer membrane failed to rescue the transport defect, proving that EMTOR must operate from the "ER side" of the interface. This finding conceptually advances our understanding of organelle transport by proposing that the motive force for mitochondria is not solely intrinsic to the organelle but is orchestrated by the ER network[31,33]. We propose that EMTOR acts as a "molecular staple," stabilizing the interaction between the mitochondrial receptor Miro1 and the cytosolic motor Kinesin-1 specifically at sites where the ER lattice contacts the mitochondrion. Furthermore, our data suggest that this scaffolding function is potentiated by liquid–liquid phase separation (LLPS). This biophysical mechanism allows the ER to rapidly concentrate dilute cytosolic motors (Kinesin-1) at specific contact sites, creating a high-density 'reaction crucible' for transport assembly. This phase-separated

compartment offers a compelling explanation for how the transport machinery achieves the high local stoichiometry required for effective motility within the crowded cytoskeletal environment.

Our biochemical mapping reveals that EMTOR exhibits exquisite specificity, binding the Kinesin-1/Miro1 axis while excluding the adaptor TRAK1. This distinction is functionally relevant: while TRAK1 overexpression can bypass EMTOR loss (likely by driving hyper-motility through an independent pathway), Miro1 overexpression cannot. This places EMTOR as a specific, obligatory co-factor for Miro1-dependent transport rather than a redundant component. The disease-causing mutation A34V further underscores this specificity; despite localizing correctly to the ER, A34V fails to bind the Miro1–Kinesin-1 complex. This suggests that the pathogenesis of SPG43 arises not from protein misfolding or aggregation, but from a precise loss of effector engagement, resulting in "empty" ER-mitochondria contacts that fail to load motors.

Finally, our data unveil a novel regulatory layer where local Ca^{2+} dynamics tune the assembly of the transport machinery. Crucially, we found that both the molecular binding affinity and the phase separation of the complex are exquisitely tuned by calcium. We identified a "bell-shaped" dependency where the EMTOR–Miro1 interaction and its co-condensation is optimal at physiological microdomain concentrations (~1–10 μM) characteristic of contact sites[27,28] but is suppressed under calcium-free or calcium-overload conditions. This relies on the calcium-sensing EF-hands of Miro1, as an EF-hand mutant became insensitive to this regulation. Physiologically, this mechanism allows the transport machinery to distinguish between the "basal" state (low affinity), the "active signaling" state (high affinity at contacts), and the "pathological overload" state (disassembly/arrest)[22,23]. In the context of HSP, this sensitivity suggests that EMTOR-mediated transport is uniquely positioned to respond to ne uronal activity patterns, and its failure may render axons unable to adapt mitochondrial distribution to metabolic demand.

In summary, we define EMTOR as an essential ER-based regulator that couples the mitochondrial transport machinery to the ER network. Our findings not only clarify the pathogenic mechanism of SPG43 but also highlight the ER–mitochondria interface as a critical command center for the logistic support of long axons.

Author Contributions

X.P. designed and conducted most of the experiments and wrote the manuscript. S.Z. conducted some molecular biology experiments, cell biology experiments, and data analysis. P.L. performed single-molecule imaging experiments. Y.W. helped with some data analysis. Y.C., X.F., X.H, Y. W., N.H., B.L. helped with the experimental design. P.Z., C.B., J.C. and J.T. are the senior authors who conceived and designed the project. All authors approved the final version of the manuscript.

Acknowledgements

The authors thank the National Center for Protein Sciences at Peking University in Beijing, China, for assistance with confocal microscopy imaging (by Chunyan Shan, Liqin Fu, Wenling Gao, and Siying Qin), flow cytometry (by Liying Du), mass spectrometry (by Dong Liu and Qi Zhang), and schematic illustrations (by Jun Hu). We thank Pathology core, school of College of Future Technology at Peking University in Beijing, China, for assistance with paraffin sample embedding, sectioning and HE staining (by Xueting Sun and Xuelian Wang). This work was supported by the National Natural Science Foundation of China (32370732, 32570806). The study was also supported in part by the Center for Life Sciences, School of Life Sciences of Peking University, the MOE Key Laboratory of Cell Proliferation and Differentiation of China, and the State Key Laboratory of Membrane Biology of China.

EXPERIMENTAL MODEL AND SUBJECT DETAILS

Animals

C57BL/6J mice (6–8 weeks old) were obtained from Beijing Vital River Laboratory Animal Technology. *EMTOR* (encoded by *C19orf12*) knockout mice were generated by Cyagen Biosciences using CRISPR–Cas9 technology. sgRNAs targeting the murine *EMTOR* gene were designed as follows: forward 5′-AAATGATTATGAGTCCAGAC-3′ and reverse 5′-TGGCGGCTTACAATCAATGC-3′. F0 heterozygous mice were backcrossed to wild-type C57BL/6J mice for two generations, and F3 heterozygotes were intercrossed to generate homozygous *EMTOR*$^{-/-}$ knockout mice. All mice were housed in specific pathogen-free (SPF) facilities at the Experimental Animal Center of Peking University. All animal procedures were conducted in strict accordance with protocols approved by the Institutional Animal Care and Use Committee (IACUC) of Peking University.

Cell culture

U2OS, HeLa, HEK-293T, and COS7 cells were cultured in Dulbecco's Modified Eagle's Medium (DMEM, CellMax, CGM101.06) supplemented with 10% (v/v) fetal bovine serum (FBS) and penicillin (100 units/mL)/streptomycin (100 μg/mL). A549 cells were cultured in Ham's F-12K (Kaighn's) medium (Meiluncell, PWL011) supplemented with FBS and antibiotics. Primary hippocampal neurons isolated from embryonic day 16.5 (E16.5) mouse brains were cultured in Neurobasal-A medium (Gibco, 10888022) supplemented with 2% (v/v) B-27 (Gibco, 17504-044) and 1% (v/v) GlutaMAX (Gibco, 35050-061). All cells were maintained at 37°C in a humidified incubator with 5% CO_2.

METHOD DETAILS

plasmids and molecular cloning

All plasmids were generated using 2X MultiF Seamless Assembly Mix (ABclonal). All DNA fragments were amplified by PCR from cDNA or genomic DNA templates. All plasmid sequences were verified using sanger sequencing (RuiBiotech).

Transfection and lentiviral transduction

For HEK293T cells, transfections were performed using Polyethylenimine (PEI; Polysciences, 23966-1) at 60% confluency. Medium was replaced 6 h post-transfection, and cells were harvested after 24 h. For other cell lines, transfections were carried out using Omni transfection reagent (EZ Biosystems, EZT-OMNI). For lentivirus production, HEK293T cells were co-transfected with the transfer plasmid, psPAX2, and pMD2.G. After 6 hours, the medium was replaced with DMEM containing 20% FBS. Viral supernatants were collected 48–72 h post-transfection, filtered, and used to infect target cells. Primary neurons were infected at DIV 3 and analyzed at DIV 8.

Generation of knockout and knock-in cell line

Gene-edited cell lines were generated using CRISPR–Cas9. The following sgRNA sequences were used for knockout cell lines:

human ***EMTOR*** (***C19orf12***) (5′-TGGGGAGAGGAAGATGAAGG-3′);

human *Miro1* (5′-TCTGGTGGAATATAGTAGTA-3′);

human *Miro2* (5′-ACAAGGTACCCGTGGTGCGC-3′);

human *TRAK1* (5′-GAATGTTGTACTTCGATCCG-3′).

For knock-in lines, donor templates were designed to tag endogenous *EMTOR* (C-terminal 3×Flag-Halo-ALFA, 5’-TGGGGAGAGGAAGATGAAGG-3’) or *Miro1* (N-terminal 3×Flag-mScarlet, 5’-TTCTTCATGTCGGCGGCTCT-3’). A549 *EMTOR* knockdown cells were generated using siRNA (5′-GCAACAGAGGCTCTTTAACGA-3′) targeting the ***EMTOR*** transcript.

Western blotting

Cells were lysed in loading buffer (50 mM Tris, pH 6.8, 1 mM DTT, 10% glycerol, 2% SDS, 0.1% Bromophenol blue), and boiled at 100°C for 10 min. Samples were run on SDS-PAGE gels (GenScript) and transferred to PVDF membranes. Membranes were blocked with 4% milk in TBST (20 mM Tris, pH 7.4, 150 mM NaCl, 0.1% Tween-20), and incubated with primary antibody at 4 °C overnight. After washing with TBST, membranes were incubated with secondary antibody at room temperature for 2 h, followed by washing with TBST. Signals were detected using SuperSignal Peroxidase Solution (Biosciences, TE0015-2) and captured on X-ray film (FUJIFILM). Band intensities were quantified using Fiji software.

Immunoprecipitation

Cells were lysed in lysis buffer (50 mM Tris-HCl, 150 mM NaCl, 1 mM EDTA, 0.5% Triton X-100, pH 7.5) containing protease inhibitor PMSF and cocktail on ice for 30 min. The cell lysates were centrifuged at 12,500 rpm for 10 minutes and supernatants were collected for input and immunoprecipitation by mixing with antibody-conjugated Protein A/G beads for 2 h at 4°C. Beads were washed five times with lysis buffer, and bound proteins were eluted in sample buffer at 100°C for 10 min for immunoblotting.

Mass spectrometry analysis of EMTOR

For mass spectrometry, HEK293T cells expressing Strep-tagged EMTOR or mouse brains (n=10) were lysed in appropriate buffers (Cell lysis: 50 mM Tris-HCl pH 7.5, 750 mM NaCl, 1% Triton X-100, 0.1 mM Biotin; Brain lysis: 50 mM Tris-HCl pH 7.5, 150 mM NaCl, 0.1% SDS, 0.5% sodium deoxycholate, 1% Triton X-100). Lysates were were centrifuged at 15,000 rpm at 4°C for 15 minutes and the supernatants were collected separately. The cell lysate supernatant was then incubated with Strep-Tactin beads for 2 h at 4°C, followed by three times beads washing with Wash Buffer 1 (50 mM Tris, 750 mM NaCl, 1% Triton X-100, pH 7.5). Mouse brain lysate supernatants were subsequently incubated with beads for 2 h at 4°C. Following incubation, beads were washed three times with Wash Buffer 1 and twice with Wash Buffer 2 (50 mM Tris, 150 mM NaCl, pH 7.5) to remove high-salt contaminants. With supernatant discarded, loading buffer was added to the beads. Eluted proteins were separated by SDS-PAGE, stained with Coomassie Blue, and excised for LC-MS/MS analysis.

Subcellular fractionation

The isolation of subcellular fractions was conducted as previously described [46]. Briefly, after collection and homogenization, cells were centrifuged for 5 min at 600g twice to remove unbroken cells and nuclei. Supernatant was collected and centrifuged for 10 min at 7,000g twice and the pellet was crude mitochondria while the supernatant was plasma membrane, lysosomes, microsomes and cytosol. The cytosol supernatant was centrifuged for 30 min at 20,000g and the supernatant was collected and further centrifuged for 1 h at 100,000g. The pellet was ER while the supernatant was cytosol. To obtain pure mitochondria, crude mitochondria pellet was suspended and centrifuged for 10 min at 10,000g to remove contaminations.

The crude mitochondrial fractions were resuspended in mitochondrial resuspension buffer and

layered on top a Percoll medium. Following centrifugation at 95,000g for 30 min, the crude MAMs fraction appeared as a diffuse white band above, while a dense band containing purified mitochondria settled near the bottom of the tube. Both MAM and pure mitochondria fractions were further centrifuged to eliminate the Percoll. All fractions obtained were rapidly frozen using liquid nitrogen and stored at − 80 °C until they were ready to be used.

RNA extraction and RNA-seq analysis

For cells, RNA extraction was conducted by using the RNA Easy Fast Tissue/Cell Kit (TIANGEN; DP451). mRNA library constructing and sequencing were performed by GENEWIZ from Azenta Life Sciences. Libraries with different indexes were multiplexed and loaded on an Illumina Novaseq instrument for sequencing using a 2×150 paired-end configuration according to the manufacturer's instructions. Raw sequencing reads in FASTQ format were processed using Fastp (v0.24.1) to remove technical sequences and low-quality bases. Clean reads were aligned to the Homo sapiens (GRCh38.107) using HISAT2 (v2.2.1). Gene-level counts were quantified using HTSeq (v0.6.1). Reads overlapping exons were counted, and multi-mapping reads or reads overlapping multiple genes were excluded. Differentially expressed genes (DEGs) were identified using DESeq2 (v1.34.0) and genes with $|\log2FC| \geq 1$ and FDR < 0.05 were classified as differentially expressed.

Prokaryotic expression, purification and *in vitro* binding assays

GST-Kif5b, GST-Miro1, EMTOR-6×His and MBP-Miro1 proteins were expressed in E. coli BL21 (DE3) induced with 1 mM IPTG at 16°C for 12–16 h. Cells were lysed using sonication in GST lysis buffer (50mM Tris-HCl, 250mM NaCl, 0.5% Triton X-100, pH=8.0), His buffer (50mM Tris-HCl, 300mM NaCl, 0.5% Triton X-100, 2mM β-Mercaptoethanol and 20mM imidazole, pH=8.0), and MBP lysis buffer (20 mM Tris-HCl, 200 mM NaCl, 1 mM EDTA, 1 mM DTT (optional), pH 7.5) followed by centrifugation at 13,500 rpm for 15 min at 4°C. The supernatant was collected and incubated with the respective affinity beads (GST-Sepharose, Ni-NTA, or Amylose resin) at 4°C with rotation for 2 hours. Beads were washed five times with wash buffer (50mM Tris-HCl, 450mM NaCl, 0.5% Tween-20, pH=7.5), and the EMTOR-6×His was eluted using His elution buffer (50mM Tris-HCl, 300mM NaCl, 0.5% Triton X-100, 2mM β-Mercaptoethanol and 250mM imidazole, pH=8.0); MBP-Miro1 protein was eluted using MBP elution buffer (20 mM Tris-HCl, 200 mM NaCl, 1 mM EDTA, 1 mM DTT (optional), 10mM maltose, pH 7.5); GST-Kif5b and GST-Miro1 protein was eluted using GST elution buffer (50mM Tris-HCl, 250mM NaCl, 50 mM GSH, pH=8.0).

For pull-down assays, purified bait proteins bound to beads were incubated with prey proteins for 2 h at 4°C. After five washes, bound complexes were eluted and analyzed by immunoblotting or Coomassie staining.

Phase separation and FRAP assays

Purified proteins were concentrated and buffer-exchanged into storage buffer (25 mM Tris-HCl pH 8.0, 500 mM KCl, 10% glycerol) using Amicon® Ultra filters (Millipore). After concentration, the protein was aliquoted and rapidly frozen in liquid nitrogen, followed by storage at −80°C. The protein concentration was determined using the BCA Protein Assay kit (Mei5bio, MF071-01). For phase separation, proteins were diluted in low-salt buffer (25 mM Tris-HCl pH 8.0, 150 mM KCl) with or without PEG8000 and $CaCl_2$ in 384-well plates. Droplets were visualized after indicated time of icubation.

For fluorescence recovery after photobleaching (FRAP) analysis of in vitro assembled condensates, particles were chosen for initial photobleaching by corresponding fluorescent-protein laser for 0.5 s with laser power 50, and the fluorescence recovery was imaged at 2 s intervals for a total of about 1 min using a Zeiss LSM980 microscope.

Immunofluorescence and imaging

Cells were fixed with 4% paraformaldehyde in PBS for 30 min at 37°C and permeabilized with 0.1% Triton X-100 in PBS for 10 min. After blocked with 4% BSA for 30 min, cells were incubated with primary antibodies at 37°C for 2 hours, and further incubated with secondary antibodies in the dark at 37°C for 1 hour, followed by three PBS washes respectively. Coverslips were mounted using a glycerol: PBS (1:1) solution containing DAPI and stored at 4°C. Imaging was performed using a Zeiss LSM980 microscope equipped with a 63×/1.4 oil objective lens in Airyscan mode. Images were acquired using ZEN software (Carl Zeiss) and processed with ZEN software or Fiji.

Proximity ligation assay

PLA (Sigma-Aldrich, DUO92101) was performed according to the manufacturer's instructions. Samples were observed under a Zeiss LSM980 confocal microscope using the Airyscan function. The total intensity of the PLA signal per cell was quantified using Fiji software.

557

558 **JC-1 staining**

559 Cells cultured in chamber slides were stained with 10 μg/mL JC-1 working solution in a 37℃, 5%
560 CO2 incubator for 15 min. After PBS wash, cells were cultured in complete medium for live cell
561 imaging. Imaging was performed using a Zeiss LSM980 microscope equipped with a 63×/1.4 oil
562 objective lens in Confocal mode. Images were acquired using ZEN software (Carl Zeiss) and
563 processed with ZEN software or Fiji.

564

565 **Mouse Behavioral Tests**

566 All behavioral tests were performed on age-matched mice trained 24 h prior to testing.

567 Hindlimb clasping: Mice were held by their tails for 10 s and scored on a scale of 0-3 based on the
568 degree of splaying outward from the abdomen. 0: the hindlimbs are fully spread and moving; 1: a
569 retraction toward the abdomen in >50% of one hindlimb; 2: a retraction toward the abdomen in >50%
570 of both hindlimbs; and 3: both hindlimbs fully retracted to the abdomen.

571 Balance beam: Mice were trained to walk across a horizontal beam (100 cm in length, 12 mm in
572 width, and 50 cm in height) to their home cages and were recorded beam-walking using a video
573 camera. Each mouse was tested three times separately.

574 Forelimb grip: Mouse was placed over the grid with its forepaws grasping the grid. Gently pull the
575 mouse backward by its tail to ensure it holds on to the upper part of the grid while maintaining a
576 horizontal torso. Record the maximum grip strength value displayed on the screen. Each mouse was
577 tested three times separately.

578 Pole test: Mice were positioned at the top of a vertical pole (50 cm high and 1 cm in diameter) and
579 assessed for their ability to descend the pole (with the snout leading) by measuring the time from the
580 initiation of the head-down movement until all four paws reached the platform. Each mouse was
581 tested three times separately.

582 Rotarod: Mice were placed on the rod of the equipment rotating at 4 rpm for habitation until
583 accelerating the rotarod from 4 to 40 rpm in 5 min. The time until falling off the beam was recorded.
584 Each mouse had a 10 min interval between trials and was tested three times per day for two
585 consecutive days.

586 Treadmill test: Mouse running ability was tested on treadmill machine (SANSBIO). The treadmill

speed was set at 5 m/min for the first 5 min, then increased to 15 m/min for another 5 min, and finally set to 21 m/min for 20 min. The test was terminated if the mouse was shocked for more than 3 s. The total running time and the number of shocks received by the mouse were recorded. Each mouse was tested once per day for three consecutive days.

Neuropathological analysis

For the collection of the adult mouse brain tissues, mice were anesthetized using Isoflurane (RWD, R510-22-10) and perfused with ice-cold PBS to flush the blood and blood cells from the brain, followed by perfusion with 4% PFA solution for fixation. The fixed samples were sent to the pathology center for paraffin sectioning, and the resulting paraffin sections were subjected to immunofluorescence staining. After dewaxing with xylene for 10 min twice, the paraffin sections were rehydrated with different gradients of ethanol (100%-95%-80%-50%-25%) for 5 min each step. They were then washed with water and boiled in 100 mM sodium citrate buffer (pH 6.0) for 10 min twice for antigen retrieval, followed by a 20 min incubation at room temperature, washed with water and PBS. The subsequent permeabilization and blocking steps were consistent with those used in cell immunofluorescence staining.

Quantification and statistical analysis

The analysis of asymmetry coefficient was conducted as previously described[34]. Quantitative data are shown in column-scattered plots (GraphPad Prism). Significance values are indicated on data plots.

References

1. Lang, B. F., Gray, M. W. & Burger, G. Mitochondrial genome evolution and the origin of eukaryotes. *Annu. Rev. Genet.* **33**, 351–397 (1999).

2. Friedman, J. R. & Nunnari, J. Mitochondrial form and function. *Nature* **505**, 335–343 (2014).

3. Suomalainen, A. & Nunnari, J. Mitochondria at the crossroads of health and disease. *Cell* **187**, 2601–2627 (2024).

4. Sheng, Z.-H. Mitochondrial trafficking and anchoring in neurons: New insight and implications. *J. Cell Biol.* **204**, 1087–1098 (2014).

5. De Vos, K. J., Grierson, A. J., Ackerley, S. & Miller, C. C. J. Role of Axonal Transport in Neurodegenerative Diseases. *Annu. Rev. Neurosci.* **31**, 151–173 (2008).

6. Wang, X. *et al.* PINK1 and Parkin Target Miro for Phosphorylation and Degradation to Arrest Mitochondrial Motility. *Cell* **147**, 893–906 (2011).

7. Blackstone, C. Cellular Pathways of Hereditary Spastic Paraplegia. *Annu. Rev. Neurosci.* **35**, 25–47 (2012).

8. Sheng, Z.-H. & Cai, Q. Mitochondrial transport in neurons: impact on synaptic homeostasis and neurodegeneration. *Nat. Rev. Neurosci.* **13**, 77–93 (2012).

9. Hirokawa, N., Noda, Y., Tanaka, Y. & Niwa, S. Kinesin superfamily motor proteins and intracellular transport. *Nat. Rev. Mol. Cell Biol.* **10**, 682–696 (2009).

10. Reck-Peterson, S. L., Redwine, W. B., Vale, R. D. & Carter, A. P. The cytoplasmic dynein transport machinery and its many cargoes. *Nat. Rev. Mol. Cell Biol.* **19**, 382–398 (2018).

11. Hancock, W. O. Bidirectional cargo transport: moving beyond tug of war. *Nat. Rev. Mol. Cell Biol.* **15**, 615–628 (2014).

12. Trivedi, D. V., Nag, S., Spudich, A., Ruppel, K. M. & Spudich, J. A. The Myosin family of mechanoenzymes: from mechanisms to therapeutic approaches. *Annu. Rev. Biochem.* **89**, 667–693 (2020).

13. Bocanegra, J. L. *et al.* The MyMOMA domain of MYO19 encodes for distinct Miro-dependent and Miro-independent mechanisms of interaction with mitochondrial membranes. *Cytoskeleton* **77**, 149–166 (2020).

14. Kang, J.-S. *et al.* Docking of Axonal Mitochondria by Syntaphilin Controls Their Mobility and Affects Short-Term Facilitation. *Cell* **132**, 137–148 (2008).

15. Zhao, Y. *et al.* Metaxins are core components of mitochondrial transport adaptor complexes. *Nat. Commun.* **12**, 83 (2021).

16. Guo, X. *et al.* The GTPase dMiro is required for axonal transport of mitochondria to drosophila synapses. *Neuron* **47**, 379–393 (2005).

17. Fransson, Å., Ruusala, A. & Aspenström, P. The atypical Rho GTPases Miro-1 and Miro-2 have essential roles in mitochondrial trafficking. *Biochem. Biophys. Res. Commun.* **344**, 500–510 (2006).

18. Stowers, R. S., Megeath, L. J., Górska-Andrzejak, J., Meinertzhagen, I. A. & Schwarz, T. L. Axonal transport of mitochondria to synapses depends on Milton, a novel drosophila protein. *Neuron* **36**, 1063–1077 (2002).

19. Glater, E. E., Megeath, L. J., Stowers, R. S. & Schwarz, T. L. Axonal transport of mitochondria requires milton to recruit kinesin heavy chain and is light chain independent. *J. Cell Biol.* **173**, 545–557 (2006).

20. Schwarz, T. L. Mitochondrial Trafficking in Neurons. *Cold Spring Harb. Perspect. Biol.* **5**, a011304–a011304 (2013).

21. van Spronsen, M. *et al.* TRAK/Milton motor-adaptor proteins steer mitochondrial trafficking to axons and dendrites. *Neuron* **77**, 485–502 (2013).

22. Wang, X. & Schwarz, T. L. The Mechanism of Ca^{2+}-dependent regulation of Kinesin-mediated mitochondrial motility. *Cell* **136**, 163–174 (2009).

23. MacAskill, A. F. *et al.* Miro1 Is a Calcium Sensor for Glutamate Receptor-Dependent Localization of Mitochondria at Synapses. *Neuron* **61**, 541–555 (2009).

24. Niescier, R. F., Hong, K., Park, D. & Min, K.-T. MCU Interacts with Miro1 to Modulate Mitochondrial Functions in Neurons. *J. Neurosci.* **38**, 4666–4677 (2018).

25. Chang, K. T., Niescier, R. F. & Min, K.-T. Mitochondrial matrix Ca^{2+} as an intrinsic signal regulating mitochondrial motility in axons. *Proc. Natl. Acad. Sci.* **108**, 15456–15461 (2011).

26. Li, Y., Yang, Z., Zhang, S. & Li, J. Miro-mediated mitochondrial transport: A new dimension for disease-related abnormal cell metabolism? *Biochem. Biophys. Res. Commun.* **705**, 149737 (2024).

27. Csordás, G. *et al.* Imaging Interorganelle Contacts and Local Calcium Dynamics at the ER-Mitochondrial Interface. *Mol. Cell* **39**, 121–132 (2010).

28. Giacomello, M. *et al.* Ca2+ Hot Spots on the Mitochondrial Surface Are Generated by Ca2+ Mobilization from Stores, but Not by Activation of Store-Operated Ca2+ Channels. *Mol. Cell* **38**, 280–290 (2010).

29. Wu, H., Carvalho, P. & Voeltz, G. K. Here, there, and everywhere: The importance of ER membrane contact sites. *Science* **361**, eaan5835 (2018).

30. Cremer, T., Neefjes, J. & Berlin, I. The journey of Ca^{2+} through the cell – pulsing through the

672 network of ER membrane contact sites. *J. Cell Sci.* **133**, jcs249136 (2020).

673 31. Rowland, A. A. & Voeltz, G. K. Endoplasmic reticulum–mitochondria contacts: function of the
674 junction. *Nat. Rev. Mol. Cell Biol.* **13**, 607–615 (2012).

675 32. Abrisch, R. G., Gumbin, S. C., Wisniewski, B. T., Lackner, L. L. & Voeltz, G. K. Fission and fusion
676 machineries converge at ER contact sites to regulate mitochondrial morphology. *J. Cell Biol.* **219**,
677 e201911122 (2020).

678 33. Friedman, J. R. *et al.* ER tubules mark sites of mitochondrial division. *Science* **334**, 358–362 (2011).

679 34. Zheng, P. *et al.* ER proteins decipher the tubulin code to regulate organelle distribution. *Nature*
680 **601**, 132–138 (2022).

681 35. Raiborg, C. *et al.* Repeated ER–endosome contacts promote endosome translocation and neurite
682 outgrowth. *Nature* **520**, 234–238 (2015).

683 36. Chen, S. *et al.* Dynamic interaction of REEP5–MFN1/2 enables mitochondrial hitchhiking on
684 tubular ER. *J. Cell Biol.* **223**, e202304031 (2024).

685 37. Kornmann, B., Osman, C. & Walter, P. The conserved GTPase Gem1 regulates endoplasmic
686 reticulum–mitochondria connections. *Proc. Natl. Acad. Sci.* **108**, 14151–14156 (2011).

687 38. Blackstone, C. Converging cellular themes for the hereditary spastic paraplegias. *Curr. Opin.*
688 *Neurobiol.* **51**, 139–146 (2018).

689 39. Denton, K. *et al.* Impaired mitochondrial dynamics underlie axonal defects in hereditary spastic
690 paraplegias. *Hum. Mol. Genet.* **27**, 2517–2530 (2018).

691 40. Meilleur, K. G. *et al.* Hereditary spastic paraplegia and amyotrophy associated with a novel locus
692 on chromosome 19. *neurogenetics* **11**, 313–318 (2010).

693 41. Landouré, G. *et al.* Hereditary spastic paraplegia type 43 (SPG43) is caused by mutation in
694 *C19orf12*. *Hum. Mutat.* **34**, 1357–1360 (2013).

695 42. Hartig, M. B. *et al.* Absence of an Orphan Mitochondrial Protein, C19orf12, Causes a Distinct
696 Clinical Subtype of Neurodegeneration with Brain Iron Accumulation. *Am. J. Hum. Genet.* **89**, 543–550
697 (2011).

698 43. Shao, C. *et al.* C19orf12 ablation causes ferroptosis in mitochondrial membrane protein-
699 associated with neurodegeneration. *Free Radic. Biol. Med.* **182**, 23–33 (2022).

700 44. Venco, P. *et al.* Mutations of C19orf12, coding for a transmembrane glycine zipper containing
701 mitochondrial protein, cause mis-localization of the protein, inability to respond to oxidative stress
702 and increased mitochondrial Ca^{2+}. *Front. Genet.* **6**, 185 (2015).

703 45. Bastian, F. B. *et al.* The Bgee suite: integrated curated expression atlas and comparative

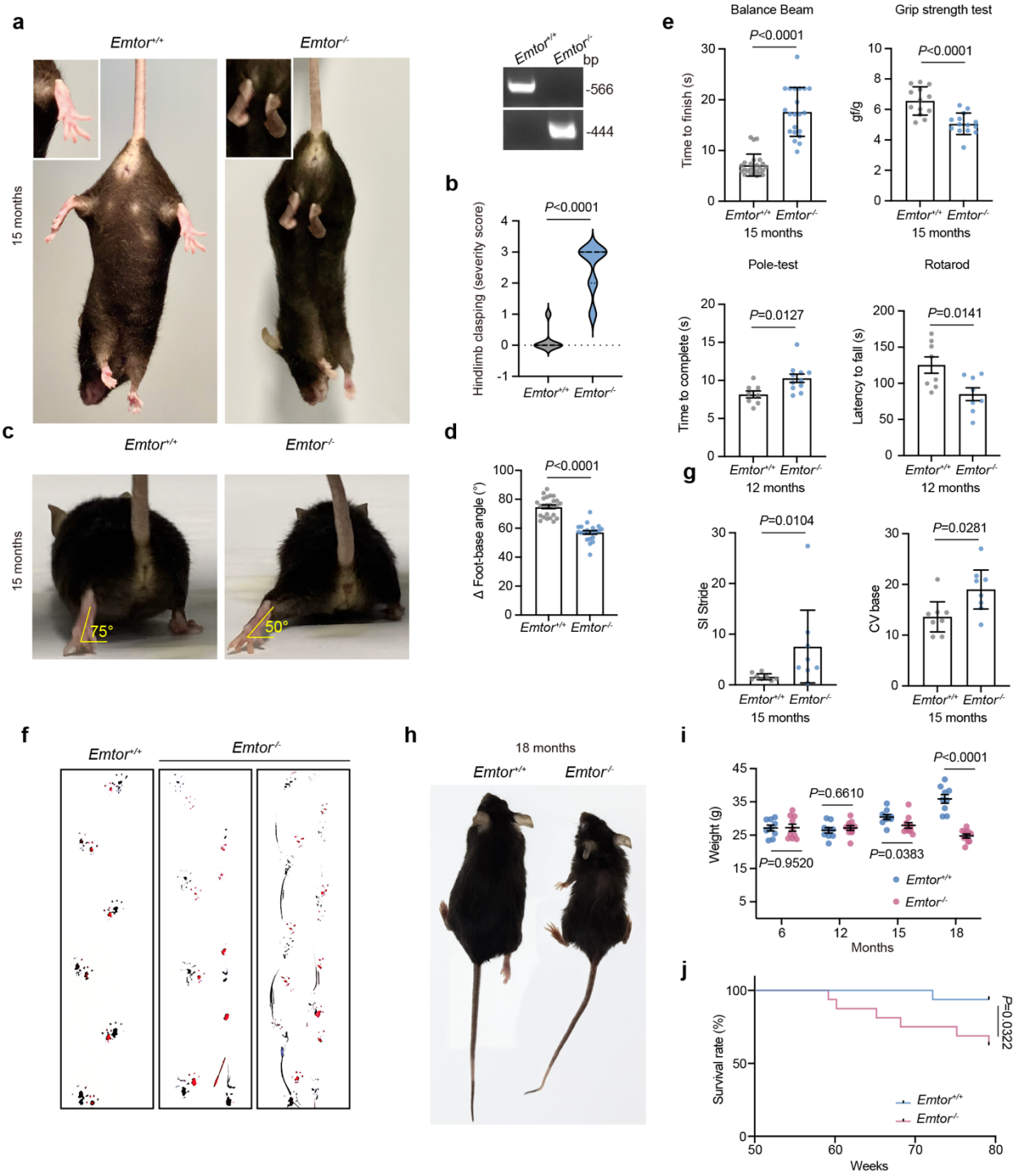

Fig. 1 | EMTOR deficiency leads to progressive motor impairment and HSP-like pathology in mice.

a, Representative images of 15-month-old *Emtor*$^{+/+}$ and *Emtor*$^{-/-}$ mice, showing hindlimb posture during tail suspension. Insets highlight hindlimb clasping. Right: Genomic PCR genotyping of tail DNA confirming the *Emtor* deletion. The wild-type allele generates a 566 bp PCR product, while the knockout allele yields a 444 bp product.

b, Violin plot showing hindlimb clasping scores (scale 0-4) in *Emtor*$^{+/+}$ and *Emtor*$^{-/-}$ mice. Each dot represents one animal. The dashed line indicates a score of 0. Statistical significance was assessed by unpaired two-tailed t-test.

c, Representative images showing hindlimb splay angles during forward locomotion in *Emtor*$^{+/+}$ and *Emtor*$^{-/-}$ mice at 15 months of age.

d, Quantification of hindlimb splay angles during locomotion shown in **c**. Each dot represents one animal. Bars indicate mean ± s.e.m. Statistical significance was assessed by unpaired two-tailed t-test.

e, Motor coordination and strength assessed by balance beam, grip strength, pole test, and rotarod assays in *Emtor*$^{+/+}$ and *Emtor*$^{-/-}$ mice at 12 months of age. Each dot represents one animal. Bars indicate mean ± s.e.m. Statistical significance was assessed by unpaired two-tailed t-test.

f, g, Representative gait traces **(f)** and quantification of gait parameters **(g)** including the stride symmetry index (SI stride, left) and step variability (CV base, right) in *Emtor*$^{+/+}$ and *Emtor*$^{-/-}$ mice. SI stride reflects left–right stride symmetry, with lower values indicating greater symmetry. CV base represents step-to-step variability and serves as a measure of gait stability. Each dot represents one animal. Bars indicate mean ± s.e.m. Statistical significance was assessed by two-tailed Mann–Whitney test.

h, Representative images of *Emtor*$^{+/+}$ and *Emtor*$^{-/-}$ mice at 18 months of age.

i, Body weight measurements of *Emtor*$^{+/+}$ and *Emtor*$^{-/-}$ mice at the indicated ages. Each dot represents one animal. Bars indicate mean ± s.e.m. Statistical significance was assessed by unpaired two-tailed t-test.

j, Kaplan–Meier survival curves of *EMTOR*$^{+/+}$ and *EMTOR*$^{-/-}$ mice. Statistical significance was assessed by log-rank test.

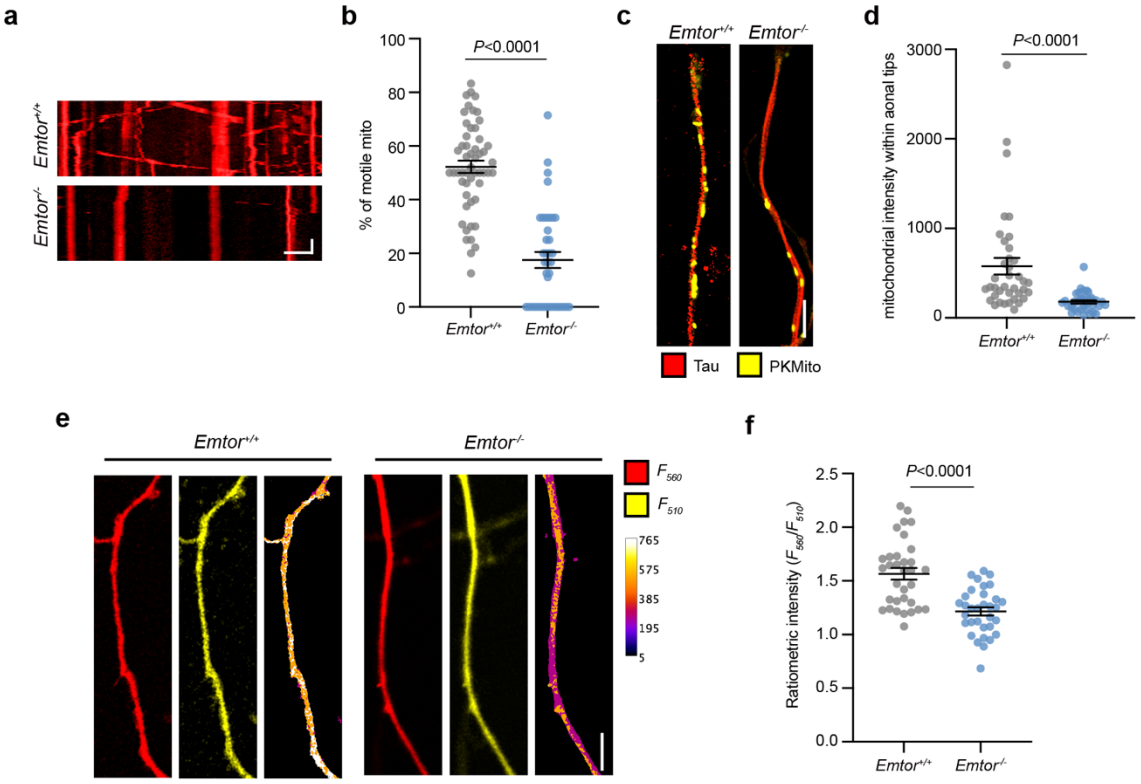

743

744 **Fig. 2 | Loss of EMTOR impairs axonal mitochondrial distribution, motility and function**

745 **a**, Representative kymographs showing axonal mitochondrial movement in *EMTOR*$^{+/+}$ and *EMTOR*$^{-/-}$ neurons.
746 Scale bars, 5 μm (horizontal) and 1 min (vertical).

747 **b**, Quantification of the percentage of motile mitochondria in axons of *EMTOR*$^{+/+}$ and *EMTOR*$^{-/-}$ neurons.
748 Each dot represents one axon. Horizontal bars indicate mean ± s.e.m. Statistical significance was assessed by
749 unpaired two-tailed t-test.

750 **c**, Representative images of axonal mitochondria labeled with PKMito in neurons derived from *EMTOR*$^{+/+}$ and
751 *EMTOR*$^{-/-}$ genotypes. Tau staining marks axons.

752 **d**, Quantification of mitochondrial intensity within axonal tips in *EMTOR*$^{+/+}$ and *EMTOR*$^{-/-}$ neurons. Each dot
753 represents one axon. Horizontal bars indicate mean ± s.e.m. Statistical significance was assessed by unpaired
754 two-tailed t-test.

755 **e,** Representative images of axonal mitochondria expressing the ratiometric mitochondrial ATP sensor
756 GoATeam2, shown as F_{560} (red), F_{510} (yellow), and pseudocolor ratio images (F_{560}/F_{510}), in *EMTOR*$^{+/+}$ and
757 *EMTOR*$^{-/-}$ neurons. Scale bars, 5 μm.

758 **f**, Quantification of ratiometric mitochondrial ATP signal (F_{560}/F_{510}) reported by the mitochondrial ATP sensor
759 GoATeam2 in axons of *EMTOR*$^{+/+}$ and *EMTOR*$^{-/-}$ neurons. Each dot represents one axon. Horizontal bars
760 indicate mean ± s.e.m. Statistical significance was assessed by unpaired two-tailed t-test.

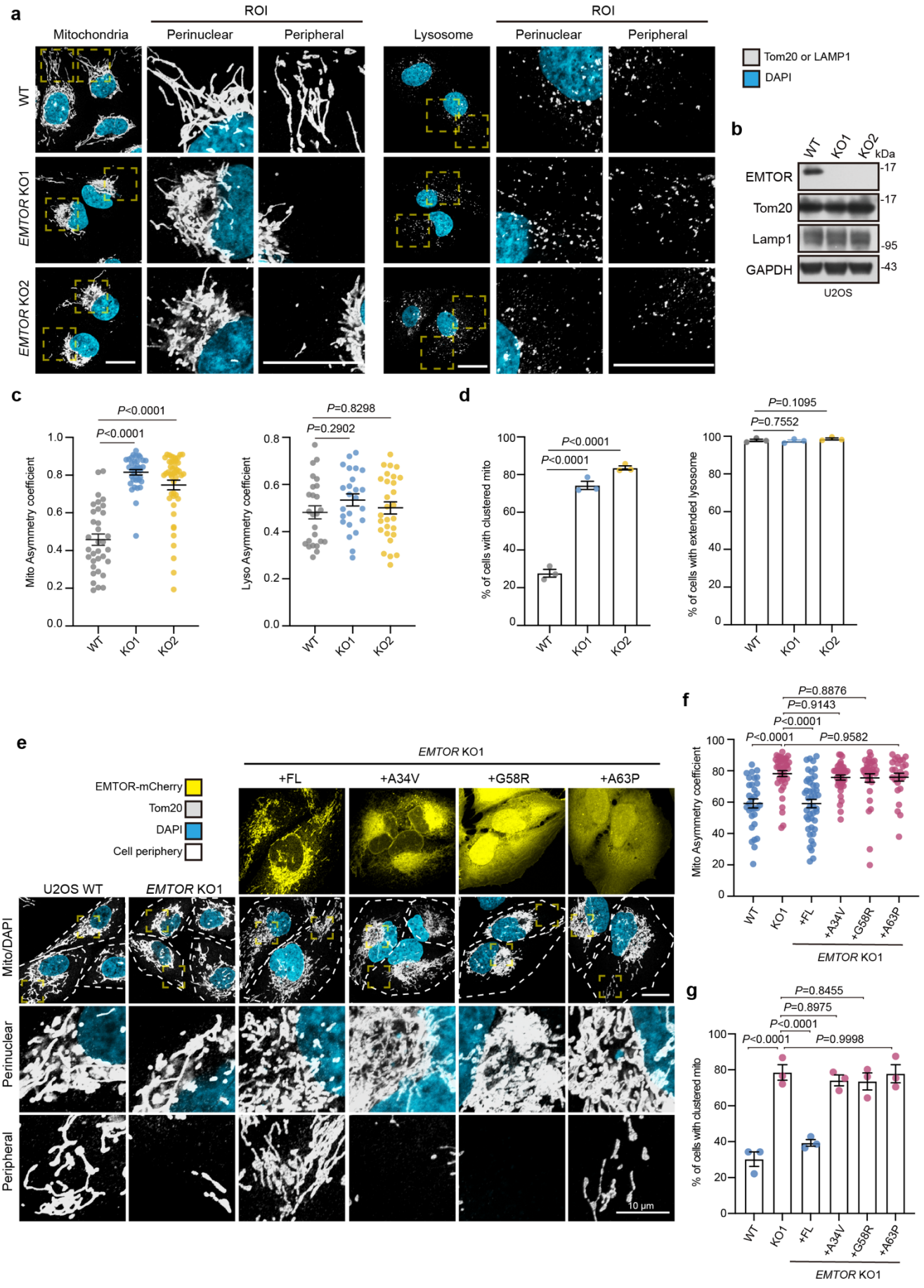

Fig. 3 | Loss of EMTOR induces perinuclear clustering of mitochondria in U2OS cells.

a, Representative confocal images of U2OS wild-type (WT) and two independent *EMTOR* knockout (KO) clones stained for mitochondria (Tom20, grey) and lysosomes (LAMP1, grey). Nuclei were labeled with DAPI (blue). Box regions indicate ROIs. Scale bars, 20 μm.

b, Immunoblot confirming loss of EMTOR in two independent KO clones. Tom20 and LAMP1 were used as mitochondrial and lysosomal markers, respectively; GAPDH served as a loading control.

c, Quantification of mitochondrial (left) and lysosomal (right) asymmetry coefficients in WT and *EMTOR* KO U2OS cells.

d, Quantification of the percentage of U2OS cells exhibiting perinuclear clustering of mitochondria (left) or lysosomes (right) following *EMTOR* knockout.

e, Representative confocal images of mitochondrial distribution in *EMTOR* KO cells re-expressing mCherry-tagged WT or mutant EMTOR (A34V, G58R and A63P). Mitochondria were labeled by Tom20 (grey) and nuclei by DAPI (Blue). Cell periphery is outlined by white dashed lines. Box regions indicate ROIs. Scale bars, 20 μm.

f, g, Quantification of mitochondria asymmetry coefficient **(f)** and percentage of cells with perinuclear mitochondrial clustering **(g)** under the indicated conditions in **e**.

All quantitative data are shown as mean ± s.e.m. In **c** and **f**, each dot represents one cell and statistical significance was assessed by one-way ANOVA with multiple comparisons. In **d** and **g**, each dot represents one biological replicate, the statistical significance was determined by Kruskal-Wallis test with multiple comparisons.

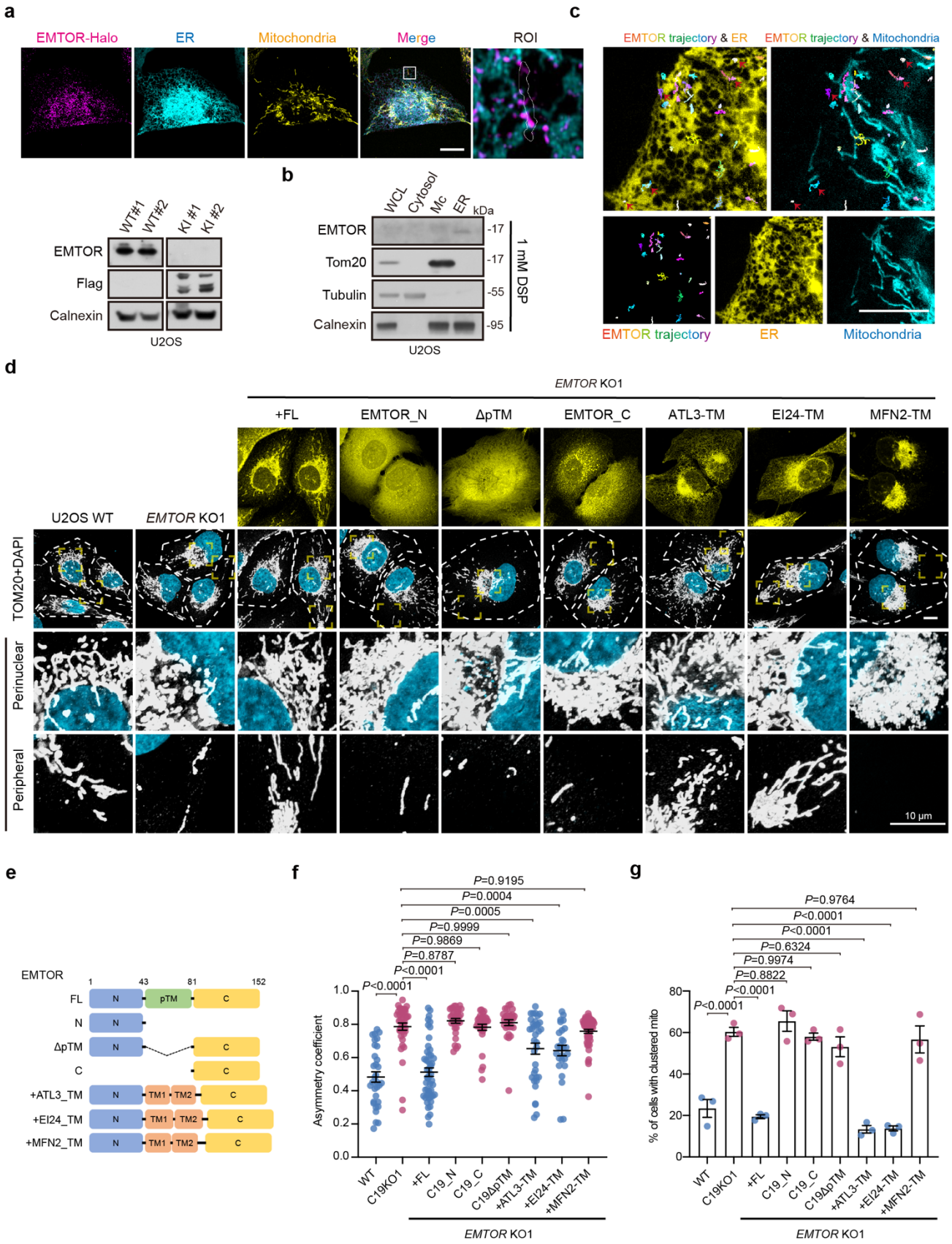

Fig. 4 | EMTOR is a dynamic ER-anchored protein enriched at ER–mitochondria contact sites, and its ER localization is essential for regulating mitochondrial distribution.

a, Representative confocal images of U2OS EMTOR–Halo knock-in (KI) cells transiently expressing the ER marker Sec61β (cyan) and stained for mitochondria (Tom20, yellow). The merged image shows EMTOR localization relative to ER and mitochondria. Boxed regions indicate ROIs shown at higher magnification. Scale bars, 20 μm. Bottom: Immunoblot confirmation of the *EMTOR*-Halo knock-in (KI) allele in U2OS clones.

b, Subcellular fractionation of U2OS cells after chemical crosslinking followed by immunoblot analysis of whole-cell lysate (WCL), cytosol, crude mitochondria (Mc) and ER-enriched (ER) fractions. Tom20, Tubulin and Calnexin were used as mitochondrial, cytosolic and ER markers, respectively.

c, Single-molecule tracking of EMTOR in U2OS EMTOR–Halo KI cells transiently expressing Sec61β (yellow) and labeled with the mitochondrial dye PKMito (cyan). Representative trajectories illustrate dynamic movement of EMTOR relative to the ER and mitochondria. Red arrows indicate EMTOR molecules moving along the ER network that do not overlap with mitochondria. Scale bar, 20 μm.

d, Representative confocal images of mitochondrial distribution in *EMTOR* KO cells re-expressing mCherry-tagged WT or the indicated truncation and transmembrane-domain chimeric constructs. Mitochondria were labeled with Tom20 (grey) and nuclei with DAPI (blue). Tubulin staining is shown as a cell morphology reference. Scale bar, 20 μm.

e, Schematic representation of the EMTOR domain deletion and chimeric constructs used for the rescue experiments in **d**. The native predicted transmembrane (TM) domain of EMTOR was deleted (ΔTM) or replaced with ER-targeting TMs (from ATL3 or EI24) or a mitochondria-targeting TM (from MFN2).

f, Quantification of mitochondrial asymmetry coefficients under the indicated conditions in **d**. Each dot represents one cell; data are shown as mean ± s.e.m. Statistical significance was assessed by one-way ANOVA with multiple comparisons.

g, Quantification of the percentage of cells exhibiting perinuclear clustering of mitochondria under the indicated conditions in **d**. Each dot represents one biological replicate, the statistical significance was determined by Kruskal-Wallis test with multiple comparisons.

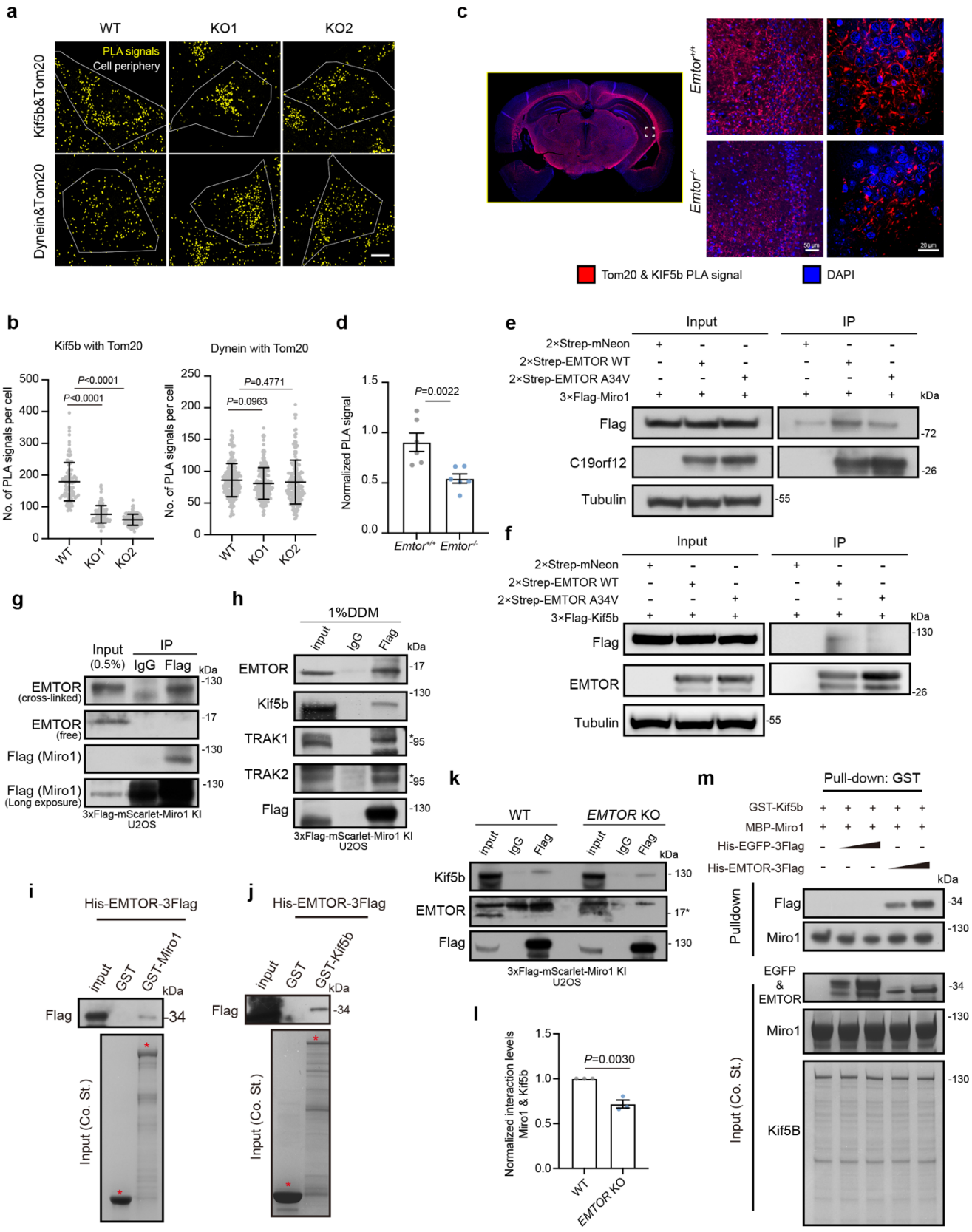

Fig. 5 | EMTOR scaffolds the assembly of the Miro1-kinesin anterograde transport complex.

a, Representative proximity ligation assay (PLA) images showing interactions between Kif5b and mitochondria (Kif5b–Tom20, top) or dynein and mitochondria (Dynein–Tom20, bottom) in U2OS WT and *EMTOR* KO cells. PLA signals are shown in yellow; cell periphery is outlined. Scale bars, 10 μm.

b, Quantification of the number of PLA signals per cell for Kif5b–Tom20 (left) and Dynein–Tom20 (right) interactions under the indicated conditions. Each dot represents one cell; horizontal bars indicate mean ± s.e.m. Statistical significance was assessed by one-way ANOVA with multiple comparisons.

c, Representative images of brain sections from *EMTOR*$^{+/+}$ and *EMTOR*$^{-/-}$ mice stained for proximity ligation assay (PLA) signals detecting Tom20–Kif5b interactions (red) and nuclei (DAPI, blue). Dashed boxes indicate regions shown at higher magnification. Scale bars, 50 μm (left), and 20 μm (right).

d, Quantification of normalized PLA signal intensity in brain sections shown in **a**. Each dot represents one animal. Bars indicate mean ± s.e.m. Statistical significance was assessed by unpaired two-tailed t-test.

e-f, Co-immunoprecipitation assays in 293T cells showing interactions between EMTOR and mitochondrial transport proteins. 2×Strep-tagged EMTOR (WT or A34V) was co-expressed with either 3×Flag–Miro1 **(e)** or 3×Flag–Kif5b **(f)**. Input and immunoprecipitated samples were analyzed by immunoblotting with the indicated antibodies.

g, Immunoprecipitation of endogenous EMTOR from U2OS cells harboring a 3×Flag–mScarlet–Miro1 knock-in, performed under DSP chemical crosslinking conditions. Input and immunoprecipitated samples were analyzed by immunoblotting to detect crosslinked and non-crosslinked forms of EMTOR and associated proteins, as indicated.

h, Immunoprecipitation of 3×Flag–mScarlet–Miro1 U2OS KI cells performed in the presence of 1% n-dodecyl-β-D-maltoside (DDM), followed by immunoblot analysis of co-precipitating EMTOR and mitochondrial transport proteins.

i, j, In vitro GST pull-down assays using purified His–EMTOR–3×Flag and GST-tagged Miro1 **(i)** or Kif5b **(j)**. Input and bound fractions were analyzed by immunoblotting for Flag. Coomassie blue staining indicates the loading of purified proteins.

k Immunoprecipitation of 3×Flag–mScarlet–Miro1 knock-in from U2OS cells in which EMTOR was subsequently deleted, followed by immunoblot analysis of co-precipitating Miro1 and Kif5b. Input, IgG and Flag immunoprecipitations are shown.

l, Quantification of normalized interaction levels between Miro1 and Kif5b in WT and *EMTOR* KO cells, based on data in **i**. Data are shown as mean ± s.e.m.; statistical significance was assessed by unpaired two-tailed t-test.

m, Competitive in vitro GST pull-down assays using GST–Kif5b and MBP–Miro1 in the presence of

844 increasing amounts of purified His–EMTOR–3×Flag or His–EGFP–3×Flag as a control. Bound fractions were
845 analyzed by immunoblotting for Flag and Miro1. Coomassie blue staining indicates protein loading.

846

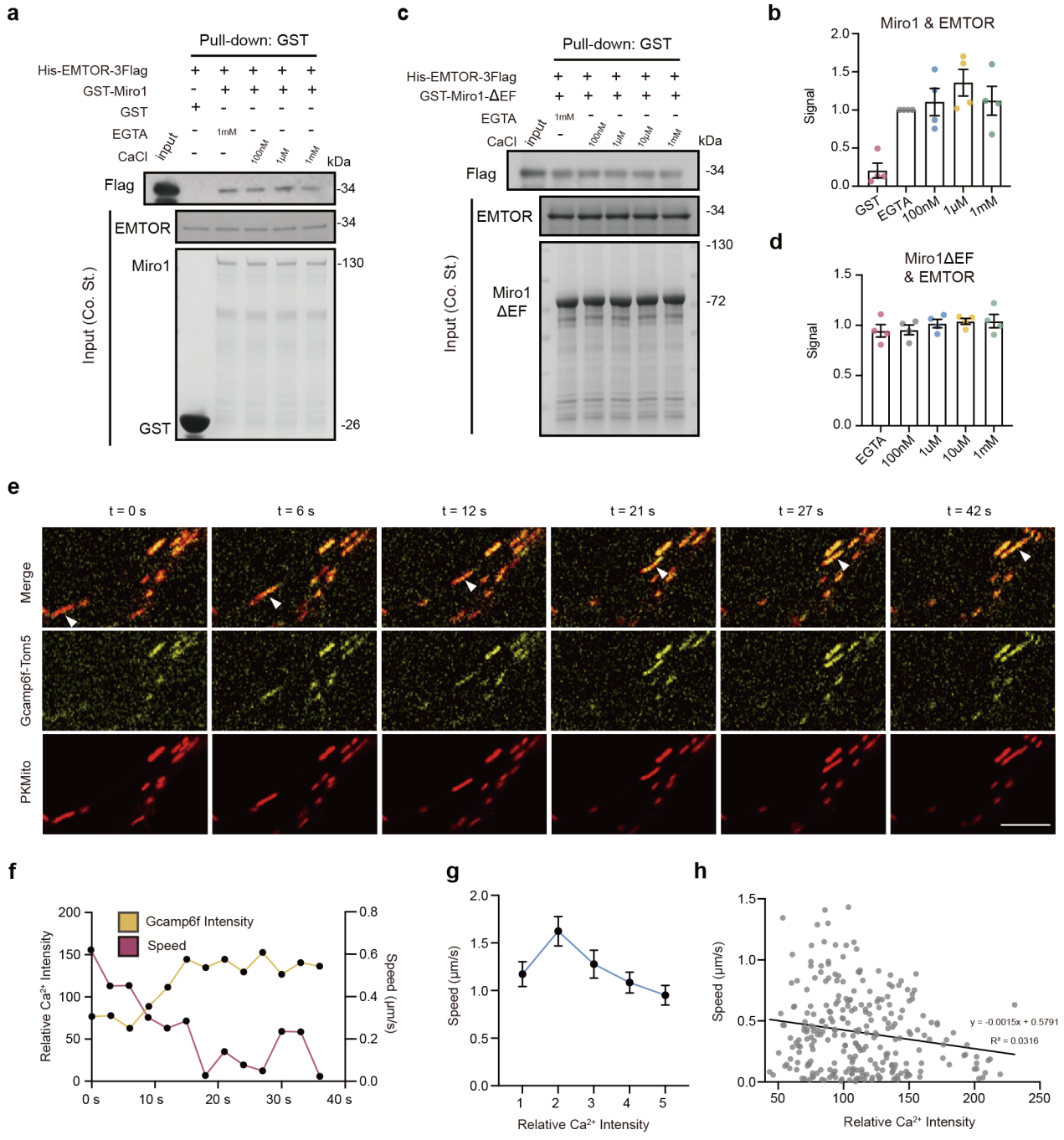

Fig. 6 | Calcium modulates the assembly of the EMTOR-Miro1 transport machinery.

a, c, In vitro GST pull-down assays examining the interaction between purified His–EMTOR–3×Flag and GST–Miro1 **(a)** or GST-Miro1-ΔEF-hand **(c)**in the presence of the indicated concentrations of $CaCl_2$ or EGTA. Input and bound fractions were analyzed by immunoblotting for Flag. Coomassie blue staining indicates protein loading.

b, d, Quantification of EMTOR–Miro1 **(b)** and EMTOR-Miro1-ΔEF-hand **(d)** interaction signals from pull-down assays shown in a, c. Data are shown as mean ± s.e.m. from independent experiments.

e, Representative time-lapse images of axonal mitochondria labeled with PKMito (red) and Ca^{2+} signals reported by transiently expressed GCaMP6f–Tom5 (yellow) in living cells. Arrowheads indicate a representative mitochondrion exhibiting a characteristic transient Ca^{2+} signal over time. Scale bars, 20 μm.

f, Representative traces showing temporal changes in relative mitochondrial Ca^{2+} intensity (GCaMP6f–Tom5) and mitochondrial movement speed from the individual mitochondrion indicated by arrowheads in d.

g, Quantification of mitochondrial movement speed grouped by relative surface calcium intensity levels. Data are shown as mean ± s.e.m. in every group.

h, Correlation analysis between mitochondrial movement speed and relative Ca^{2+} intensity. Each dot represents one mitochondrion at one timepoint; the fitted line indicates linear regression.

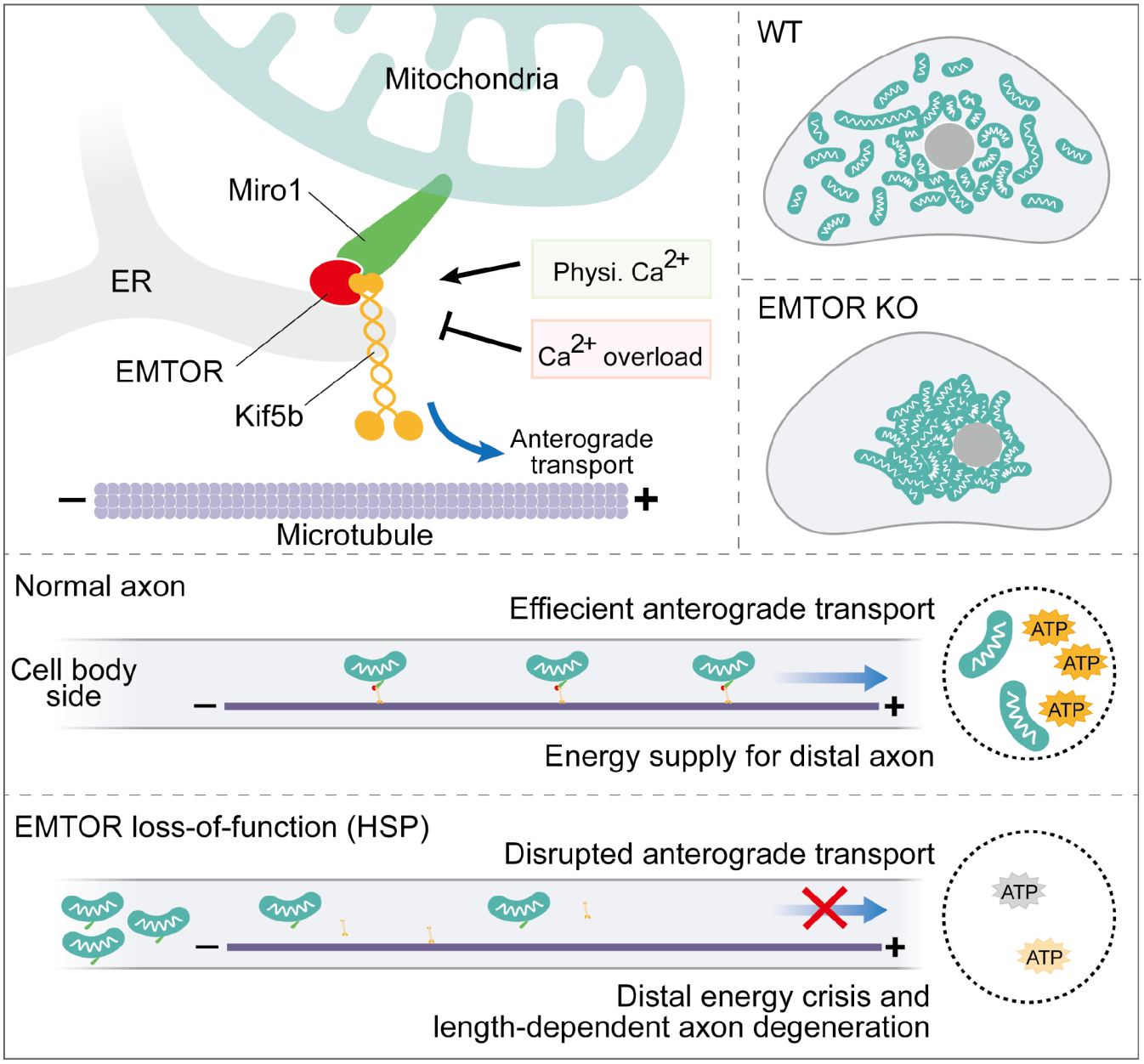

Fig. 7 | Proposed model: EMTOR acts as an ER-anchored scaffold to orchestrate mitochondrial transport.

EMTOR molecular mechanism at ER-Mitochondria contact site (Top left). Under physiological conditions, EMTOR is dynamically anchored to the ER membrane at ER–mitochondria contact sites. It functions as a specialized scaffold that bridges the ER to mitochondria, promoting the assembly of mitochondrial transport complex formed by mitochondrial outer membrane protein Miro1 and the anterograde motor Kinesin-1 (Kif5b). Importantly, this assembly is modulated by local Ca^{2+} levels, being optimal at physiological concentrations found at contact sites but significantly weakened under calcium overload.

Cellular regulation of mitochondrial distribution (Top right). In wild- type cells (top), EMTOR promotes the peripheral distribution of mitochondria. In the absence of EMTOR (middle), the outward transport machinery is compromised, leading to severe mitochondrial perinuclear clustering.

Neuronal consequences and HSP pathology (Bottom): In physiological conditions, EMTOR-mediated transport ensures the robust delivery of mitochondria to distal axonal terminals, maintaining high local ATP levels required for synaptic homeostasis. In pathological conditions, the failure of EMTOR-dependent transport leads to a progressive depletion of mitochondria at the distal axon. This results in a local energy crisis (low ATP) at synaptic terminals, driving the "dying-back" length-dependent axonopathy characteristic of Hereditary Spastic Paraplegia (HSP).